Engineering Structures 259 (2022) 114146

Contents lists available at ScienceDirect

Engineering Structures

journal homepage: www.elsevier.com/locate/engstruct

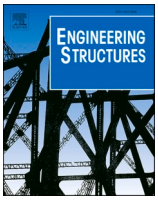

Innovative prefabricated lightweight slab system of high structural performance

Joaquim A.O. Barros [a,*], Inês G. Costa [b], Cristina M.V. Frazão [b], Tiago D.S. Valente [b], Lúcio A.P. Lourenço [b], Felipe J.S.A. Melo [b]

[a] Universidade do Minho, ISISE, Dep. Engª Civil, Guimarães, Portugal
[b] CiviTest, Jesufrei, Vila Nova Famalicão, Portugal

ARTICLE INFO

Keywords:
Fibre reinforced concrete
Cold formed steel sheets
Slab system
Structural performance
Design approach

ABSTRACT

This paper presents a new pre-fabricated lightweight slab system where the relatively high post-cracking tensile capacity of steel fibre reinforced concrete (SFRC) is combined with the high ductility and tensile strength of optimized shape profiles made by cold formed steel sheets for a synergetic result in terms of structural performance. The SFRC fills the longitudinal steel profiles (girders) that have openings in the web for materializing SFRC shear mechanisms that provide very high shear resistance to the slab. This slab system (designated by PreSlabTec) includes a SFRC deck of 40 mm thickness and lightweight blocks serving as permanent moulds to the SFRC and thermal insulation. The transversal stiffness is assured by thin wall tubular steel profiles that remained anchored in the girders due to their openings. PreSlabTec is simple and fast of executing and was conceived for being produced in an automation process of prefabrication industry.

For assessing the performance of the PreSlabTec in serviceability and ultimate limit state conditions, an extensive program with almost real scale prototypes was executed and tested under loading configurations for flexural and shear failures. For the flexural loading configurations, the PreSlabTec demonstrated a very high load carrying capacity and ductility performance. The PreSlabTec never failed in shear, despite the very exigent shear loading configurations adopted. The long-term deflection was also experimentally evaluated for the standard design requirement for slabs of residential buildings, and a relatively low average creep coefficient of 0.13 was obtained.

Finally, the theoretical approach for the design of PreSlabTec is described and its good predictive performance is demonstrated.

1. Introduction

The higher post-cracking tensile capacity provided by fibre reinforcement to cement based materials is being explored for reducing, or even eliminating, conventional steel reinforcements in flooring [1], road pavements [2], tunnelling [3–6], prefabricated concrete structural applications [7–9], elevated slabs [10–12], or for developing new constructions systems [13,14], in an attempt of producing more cost competitive and sustainable built environment.

One of the main applications of fibre reinforcement is in the replacement of steel stirrups [8,15–20] due to the relatively large time required on the preparation and application of this type of reinforcement, and the restrictions it imposes for decreasing the thickness of beam's web, due to the required concrete cover protection against corrosion effects. In fact, there is evidence of the possibility of eliminating conventional steel stirrups without the occurrence of brittle shear failure in real scale FRC structures, as long as an adequate high post-cracking tensile capacity is assured for the FRC [8,9,15–17]. In the major part of these structural applications, conventional longitudinal reinforcement, applied passively or with a certain prestress level, is used for assuring the aimed flexural capacity. This reinforcement has also a favourable effect on the shear resistance due to dowel effect and its influence on the aggregate interlock mechanisms. This last mechanism is mainly significant when the flexural reinforcement is applied with a certain prestress [8,9,16]. Due to the susceptibility of these steel flexural reinforcements to corrosion, attempts are being made for their replacement by fibre reinforced polymer (FRP) systems [21–26]. However, due to the susceptibility of FRP to high temperatures [27,28],

* Corresponding author.
E-mail address: barros@civil.uminho.pt (J.A.O. Barros).

https://doi.org/10.1016/j.engstruct.2022.114146
Received 28 September 2021; Received in revised form 10 February 2022; Accepted 12 March 2022
Available online 23 March 2022

hybrid flexural reinforcements (FRP and steel) have been used [9,29–32], where FRP have the minimum concrete cover thickness for assuring their required bond conditions, while steel reinforcements are disposed with a larger concrete cover thickness for better protection to corrosion and in a percentage sufficient to avoid collapse in case of a fire [9], since it is assumed that FRP reinforcements lose their functionality in a fire scenario [24–26]. By using FRC for eliminating the steel stirrups, I shape cross section beams of relatively large size and 70 mm web's thickness, flexurally reinforced with a hybrid passive/prestressed FRP-steel system, were tested up to their failure with notable load carrying and deflection capacity [9]. The use of fibres as a shear reinforcement and for improving the FRP-concrete bond performance of structural elements flexurally reinforced with FRP bars has been demonstrated capable of enhancing the behaviour of this type of elements at serviceability limit state conditions (stiffness, cracking, deflection and stress level in the FRP bars), as well as at ultimate limit state conditions by assuring more ductile failure modes [33–36].

Regarding concrete slab systems, the use of FRP as flexural reinforcement is already quite current, not only for new constructions where corrosion of steel bars is a serious concern [22–26], but also for the rehabilitation and strengthening of existing concrete structures, especially in decks of bridges, sometimes combined with FRC for better cracking control [37]. FRP slab systems based on the concept of sandwich panels have been explored, where the stiffer and stronger components are disposed in the outer layers and the core is formed by FRP grids and/or engineered foams [38–42]. These very lightweight slabs are mainly dedicated to the structural rehabilitation of pavements, in locations where elevation of heavy construction systems is not possible or is too time consuming and costly. Some of these FRP-based slab systems include a compression layer in FRC [43] to avoid premature failure of the FRP part in compression (local buckling or wrinkling failure mode with very deficient mobilization of the tensile capacity of the FRP part in tension [42]). As long as proper bond between the FRC layer and FRP substrate is assured, the relatively large deformation of FRC in compression allows the development of large curvature, improving the pseudo-ductility of this type of slab systems [44].

By combining FRP profiles produced by the pultrusion technique with a thin compression deck in FRC, very lightweight pedestrian bridges of simple and fast application have been developed, without any element susceptible to corrosion [45]. However, the relatively high depth of these FRP profiles for attending the design verification for serviceability limit states due to deflection and vibrations, and their consequent high costs, do not allow the use of this material concept for slab systems in residential and commercial buildings.

Thereby, in the present paper, a new prefabricated lightweight slab is proposed, and its structural performance assessed, where instead of using FRP pultruded profiles for the longitudinal girders, profiles made by cold formed steel sheets and with engineered openings in their webs are adopted for being filled with FRC. When filling the girders of this slab system, a very thin deck of FRC is also cast. Prefabricated blocks in polystyrene serve as permanent moulds for the casting process of the FRC and also as thermal insulation. The transversal stiffness of this slab system is assured by thin wall tubular steel profiles that are anchored in the longitudinal girders, due to the openings in the profiles of these girders. The very high flexural and shear capacity of this slab, and outstanding ductility despite its relatively low self-weight, are demonstrated in this paper by performing experimental tests with almost real scale prototypes subjected to different flexural and shear loading configurations. The long-term deflection of this very effective composite slab system is also assessed experimentally, by determining its creep coefficient. Finally, the theoretical approach developed for the design is presented and its adequate predictive performance is demonstrated.

2. Experimental program

Throughout the experimental program, the same slab prototype geometry was adopted (see Fig. 1). The slab prototype has a nominal total length of 4600 mm and a nominal width of 1227 mm, corresponding to a slab panel of 5.64 m^2. It is composed by two girders, placed 983 mm from each other (center-to-center). Each girder is composed of a 3 mm U-shaped steel sheet, which acts both as stay-in-place formwork for the FRC that fills the girder, as well as longitudinal and shear reinforcement. The steel sheet exhibits laser cut hexagonal openings on the vertical faces of the U-shape, from which the FRC flows during the filling operation, forming a 30 mm stiffener on the outer surface of the steel sheet. The prototype possesses a permanent insulated filling (extruded polystyrene, XPS) between the girders, which also acts as mould to shape the FRC stiffeners and compression deck layer.

The hybrid FRC-U-shaped steel sheet girders have a height of 180 mm, while the concrete nominal deck thickness is 40 mm; the total height of the prototype is 220 mm. To guarantee the stability of the prototype during handling and to provide transversal stiffness, the first and last hexagonal openings of each girder are coupled with embedded hollow steel profiles of cross-section 50 × 90 mm^2 and thickness of 4 mm.

The span length of these prototypes is a compromise between being representative of the most current span length of slab systems existing in the market for residential buildings and the testing space of the adopted reaction frame. The width of the cross section of the prototypes aims to optimize the space occupied by these elements when transported in the type of trucks used to transport prefabricated structural elements, and also takes into consideration the flexural capacity of the relatively thin SFRC deck regarding the distance between girders.

3. Material properties

Due to the large amount of concrete necessary to produce the specimens, the average concrete properties were determined by an independent experimental program. The concrete specifically developed for these elements uses 413 kg/m^3 of Portland cement CEM I 42.5R and is reinforced with 60 kg/m^3 of hooked ends steel fibres (fibre length = 60 mm, aspect ratio = 80 and tensile strength of approximately 1100 MPa). The average compressive strength in cubes ($f_{cm,cub}$) and cylinders ($f_{cm,cyl}$), the modulus of elasticity (E_{cm}), the limit of proportionality (f_{LOP}) and the residual flexural tensile strength parameters in bending (f_{Ri}, i = 1 to 4) obtained for the FRC at different ages are presented in Tables 1–4.

The girder is fabricated from 3 mm steel sheets (S275JR). The yield strength (f_{sy}) and ultimate strength (f_{su}) were obtained by testing 3 samples with 40 mm of width and 300 mm of length. Although the steel strain during the tensile test was not possible to be measured, the elongation after fracture (ε_{su}) was determined by the manual procedure defined in ISO 6892–1:2019. The obtained results are presented in Table 5.

4. Monotonic tests

In this experimental campaign, four types of tests were carried out. For simplification purposes, the tests are referred to as Xn, where X is a letter describing the test type (B, for bending and S, for shear), and n is a number that indicates the test span, in millimetres. The following tests are reported in this paper:

- Test B4400: 4-point bending test with a distance between supports of 4400 mm;
- Test B2400: 3-point bending test with a distance between supports of 2400 mm;
- Test S800: 3-point shear test with a distance between supports of 800 mm;
- Test S1200: 3-point shear test with a distance between supports of 1200 mm.

As a control property, 150 mm cubes were collected during the

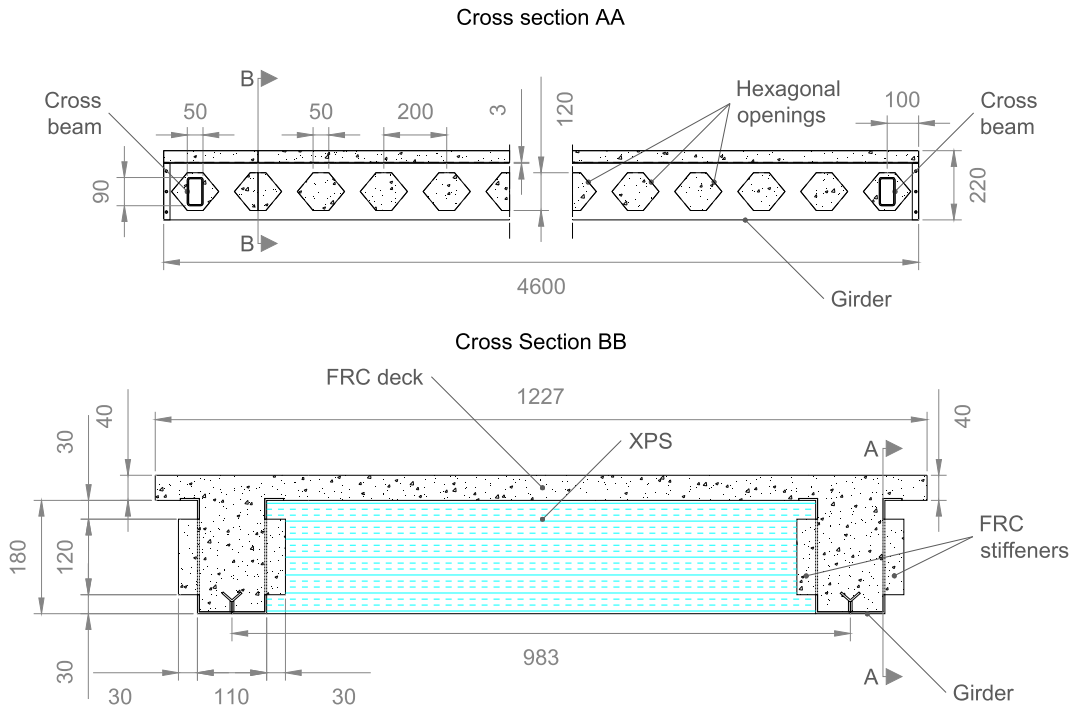

Fig. 1. Prototype geometry and dimensions (in millimetres).

Table 1
Average compressive strength in 150 mm cubes (NP EN 12390–3:2019).

Age	No. of samples	Average strength, $f_{cm,cub}$ [MPa]	Standard deviation [MPa]	CoV [%]
3	4	39.6	0.7	1.8
7	4	51.6	1.4	2.7
14	4	58.8	2.0	3.4
28	4	61.7	0.8	1.4
90	4	64.3	1.2	1.8

Table 2
Average compressive strength in cylinders (NP EN 12390–3:2019).

Age	No. of samples	Average strength, $f_{cm,cyl}$ [MPa]	Standard deviation [MPa]	CoV [%]
3	3	37.0	0.3	0.9
7	3	46.3	0.8	1.8
14	3	52.7	0.2	0.3
28	6	55.8	2.2	3.9
90	3	61.9	0.7	1.1

Table 3
Average secant elasticity modulus in 150 mm cylinders (NP EN 12390–13:2014).

Age	No. of samples	Average elasticity modulus E_{cm} [GPa]	Standard deviation [GPa]	CoV [%]
3	3	22.3	1.0	4.3
7	3	26.3	1.7	6.4
14	3	27.4	0.5	1.7
28	6	28.4	1.1	3.9
90	3	30.5	0.8	2.5

production of the prototypes for assessing the compressive strength variation of the FRC batches. In the B4400 prototype, the average compressive strength at 28 days was 45.8 MPa, while in the remaining tests the average compressive strength was 64.5 MPa (values at 28 days of FRC age).

Table 4
Average LOP and residual strength in notched beams at 28 days (EN 14651:2005 + A1:2007).

No. of samples	Property	Average strength [MPa]	Standard deviation [MPa]	CoV [%]
9	f_{LOP}	4.87	0.40	8.2
	f_{R1}	7.11	1.85	26.0
	f_{R2}	7.75	1.87	24.1
	f_{R3}	6.94	1.71	24.6
	f_{R4}	6.17	1.51	24.5

Table 5
Steel sheet properties (ISO 6892–1:2019).

No. of samples	Property	Average strength	Standard deviation	CoV [%]
3	f_{sy} [MPa]	289	7	2.3
	f_{su} [MPa]	371	3	0.7
	ε_{su} [‰]	341	40	12

In all the tests, the deflection was monitored in several positions of the slab prototype, as well as the strains in the bottom face of the girder (steel tensile strain) and in the top face of the FRC deck (concrete compressive strain), as shown in Fig. 2. The strains installed on the bottom face of the girder (on the steel surface) and on the top surface of the FRC deck were measured by electric strain gauges with 30 mm and 60 mm gauge length, respectively. Additionally, in the tests with the prototypes B2400, S800 and S1200, the strain state of the lateral FRC stiffener was also monitored. This was made by using delta rosettes, as proposed elsewhere [46]. Since two rosettes are installed in each test, the rosette pointing upwards will be referred as delta (Δ) rosette (closer to the loaded section), while the rosette pointing downwards will be referred as nabla (∇) rosette. The strains in the rosettes were measured by installing in each rosette arm a proximity sensor with a 4 mm range. Although the full rosette arm size is 100 mm, each sensor has monitored the deformation of a 75 mm reference length.

Note that the right support on the test setup of B2400, S800 and

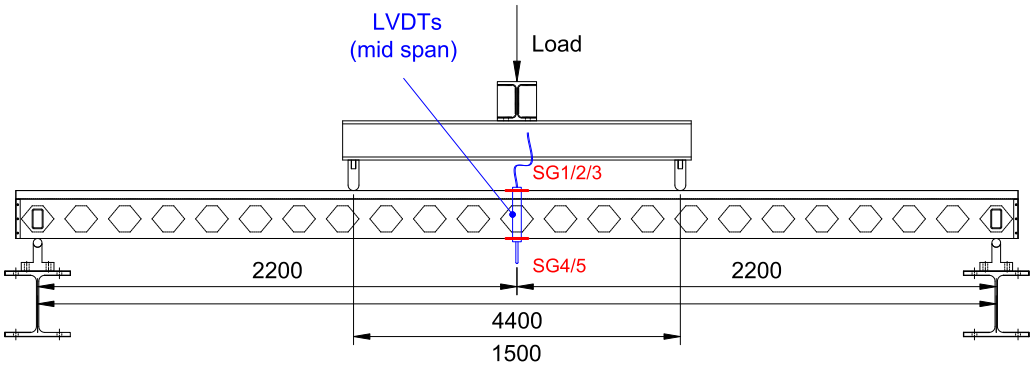

(a)

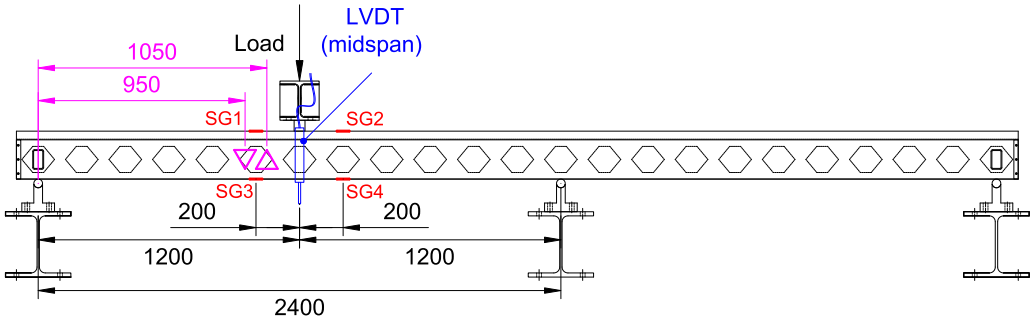

(b)

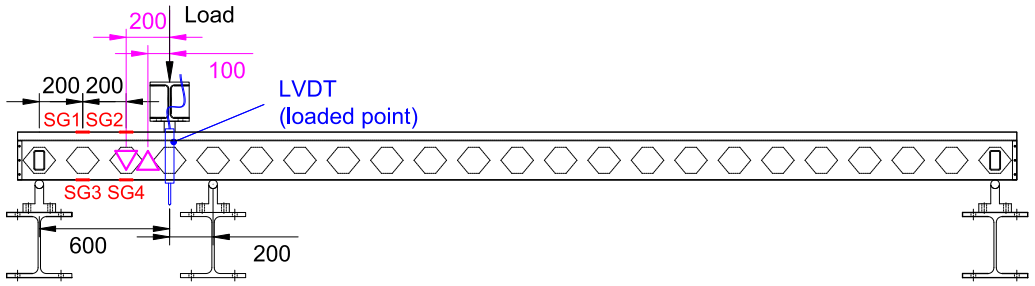

(c)

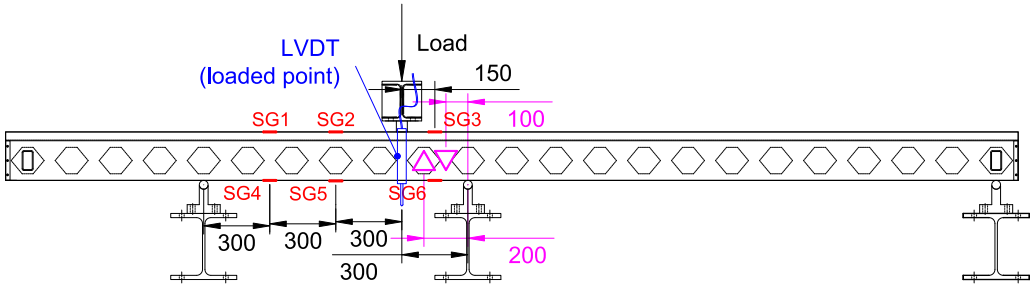

(d)

Fig. 2. Test configurations (dimensions in millimetres): (a) Test B4400; (b) Test B2400; (c) Test S800 and (d) Test S1200.

S1200 does not restrict the uplift of the prototype in this section, so only the self-weight of the prototype part out of the testing span affects the reactions in the other supports, whose amount is very small regarding the ultimate applied loads.

The first bending test (B4400) was controlled by a servo-actuator equipped with a load cell of 500 kN maximum capacity. The test velocity was 25 μm/s (controlled by the internal transducer of the actuator). To prevent the dislocation of the two loaded points during this test, the rounded steel profiles used to transfer load are bolted to a grid of steel profiles (see Fig. 3a). The remaining tests were controlled by a different servo-actuator, equipped with a load cell of 2000 kN maximum capacity. In these tests, load was transmitted to the slab prototype by means of a steel profile of 50 × 50 mm^2 cross section (see Fig. 3b/c/d). The adopted deflection velocity was 20 μm/s in second bending test (span = 2400 mm) and 5 μm/s in both shear tests.

4.1. Deflection

The relationship between the force at the loaded section and its corresponding deflection is represented in Fig. 4 for each tested prototype. The ordinate axis corresponding to the force is different amongst the tested prototypes since it was adopted the criterion of having the same ordinate axis of the bending moment at the loaded section in all the prototypes.

In the prototypes B4400 and B2400, the force–deflection response is characterized by the following phases: 1) linear-elastic; 2) elasto-cracked of relatively high amplitude and small loss of stiffness regarding the previous phase; 3) elasto-plastic-cracked with significant hardening and very high ductile behaviour. In the B2400, above the deflection of about 35 mm, this prototype entered in a structural softening stage, indicating the flexural capacity of the prototype's cross section is 117.3 kN.m. It is interesting to note that, considering the flexural capacity of the B4400 prototype when it was interrupted, it supports an equivalent live load (uniform distributed load inducing the same maximum bending moment) of approximately 44 kN/m^2.

Regarding the behaviour of the S800 and S1200 prototypes, both tests were interrupted when the maximum load carrying capacity of the reaction frame was attained (≅ 500 kN). However, at this stage no sign of shear failure occurrence was visible. Furthermore, the force–deflection response of the S1200 has entered in a significant nonlinear phase, indicating the initiation of yielding of the steel profile, demonstrating the excellent shear strength capacity of the PreSlabTec system.

The total applied force and the deflection (middle span section for the B4400 and at loaded section in the remaining prototypes) at concrete crack initiation, at steel yield initiation and at peak load are presented in Table 6, as well as the force at deflection levels of $l/250$ and $l/500$, where l is the prototype's span length. The deflections corresponding to $l/250$ and $l/500$ define the interval recommended by EC2 [47] for the verifications of serviceability limit state conditions in slabs applications. Apart from the B4400 prototype, in the other prototypes the deflection at yield initiation was less than the deflection corresponding to $l/250$, and even the deflection corresponding to $l/500$ in the S-type prototypes.

From the results in the B-type prototypes it is verified that the ratio of the deflection at maximum and at steel yielding is higher (since the load carrying capacity of B4400 was still increasing when the test was interrupted) than 5.3, demonstrating the high level of ductility of the

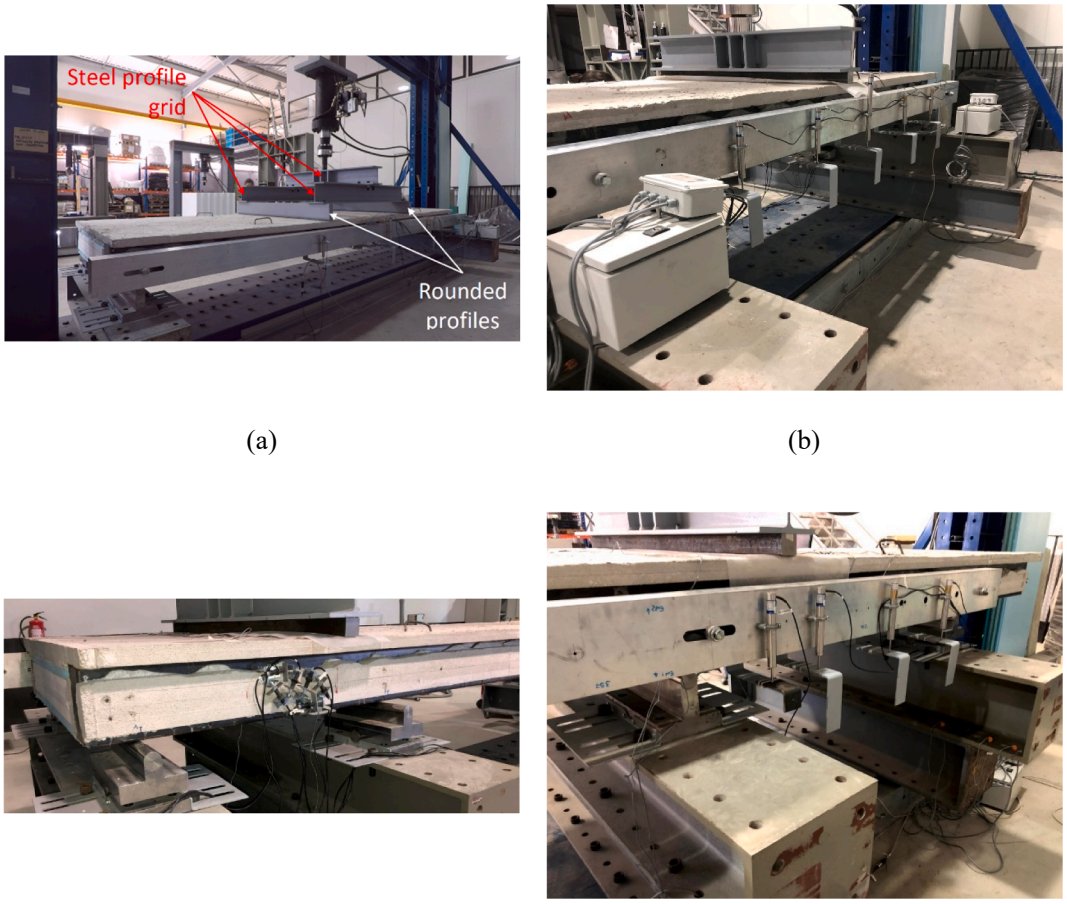

Fig. 3. Photographs of the test configurations: (a) B4400; (b) B2400; (c) S800 and (d) S1200.

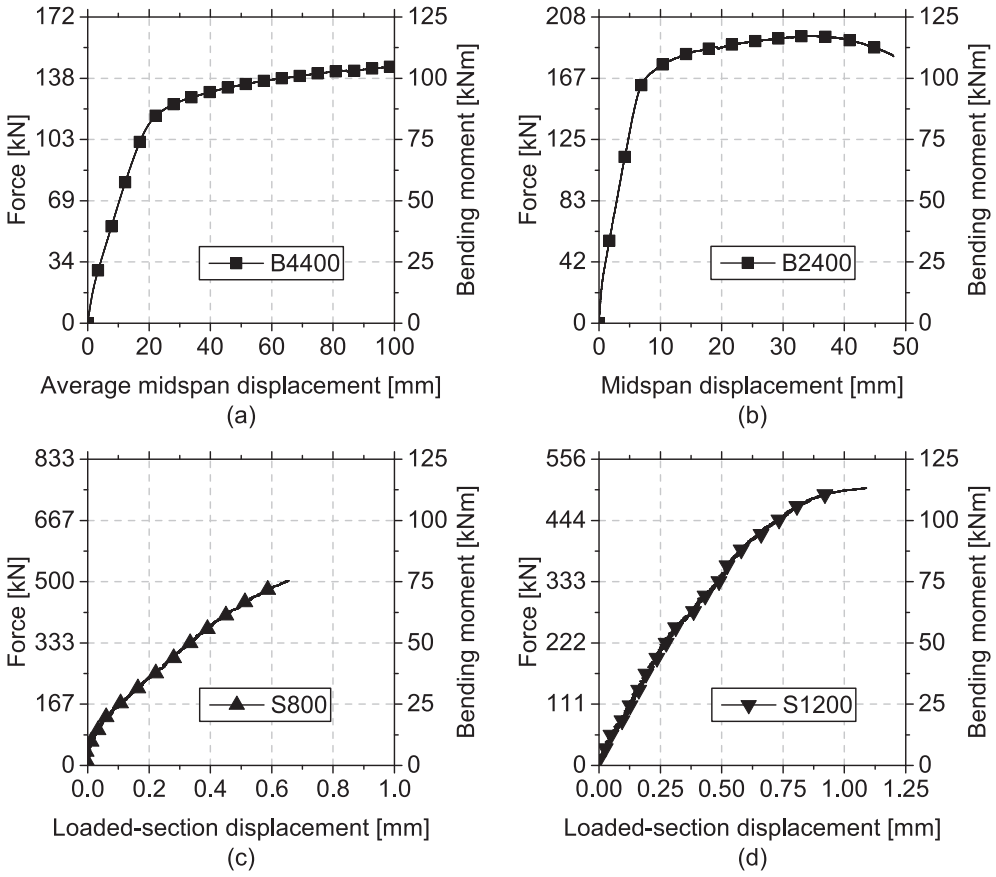

Fig. 4. Load and bending moment versus loaded-section displacement: (a) Test B4400; (b) Test B2400; (c) Test S800 and (d) Test S1200.

Table 6
Summary of the displacement and forces in the slab prototypes.

Parameter	Test	Concrete cracking	Steel yielding	Maximum	$l/500$	$l/250$
Displacement * [mm]	B4400	1.58	20.0	106	8.80	17.6
	B2400	0.53	6.36	34.4	4.80	9.60
	S800	0.04	NA	NA	1.60	3.20
	S1200	0.11	1.62	NA	2.40	4.80
Applied force [kN]	B4400	17.1	112	146	60.5	104
	B2400	28.1	156	196	126	174
	S800	97.0	NA	503**	NA	NA
	S1200	63.5	437	503**	NA	NA

NA: not applicable.
* The displacements refer to the mid-span in test B4400 and to the loaded-section in all other tests.
** The indicated force is the maximum load carrying capacity of the reaction frame.

PreSlabTec.

Table 7 presents the elastic flexural stiffness, EI_{el}, which was evaluated according the following equations for the different test setup:

$$EI_{el} = P_{crack}a\left(3l^2 - 4a^2\right)/(48\delta_{crack}) \quad \text{for B4400} \tag{1}$$

$$EI_{el} = P_{crack}l^3/(48\delta_{crack}) \quad \text{for B2400} \tag{2}$$

$$EI_{el} = P_{crack}a^2(l-a)^2/(3\delta_{crack}\cdot l) \quad \text{for S800 and S1200} \tag{3}$$

where P_{crack} and δ_{crack} are the load at crack initiation and the corresponding deflection (values indicated in Table 6), and a (shear span) is the distance between the leftmost support and the leftmost loaded section. As expected, the EI_{el} decreases with the decrease of the shear span due to the higher contribution of the shear stiffness for the deflection at crack initiation. The S800 is an exception, which should be caused by the smaller length of the shear spans (Fig. 2c), a_{left}/h=600/220 ≅ 2.7, a_{right}/h=200/220 ≅ 0.9, where h is the total height of the prototype, which has promoted the conduction of the applied load to the supports,

Table 7
Summary of the mechanical properties of the tested slab prototypes.

Test	EI_{el} [kNm^2]	Bending moment [kNm]			Shear forces [kN]	
		FRC Cracking,M_{cr}	Steel Yielding,M_y	Maximum,M_{max}	Left support	Right support
B4400	16,239	12.4	81.3	106.0	73	73
B2400	15,269	16.9	93.5	117.3	98	98
S800	14,550	14.6	–	75.4	125.75*	377.25*
S1200	11,690	14.3	98.4	113.2	125.75*	377.25*
Average	14,437	14.5	91.1	103.0	–	–
Standard deviation	1958	1.85	8.80	18.96	–	–
CoV[%]	14	13	10	18	–	–

* Do not represent the shear capacity, since the corresponding tests were interrupted due to the attainment of the load carrying capacity of the reaction frame.

contributing to the relative increase of P_{crack} and decrease of δ_{crack}.

Regarding the bending moment at crack and steel yield initiation, M_{cr} and M_y, respectively, and at maximum load, M_{max}, apart the case of S800 where steel yield initiation did not occur when the test was interrupted due to the attainment of the load carrying capacity of the reaction frame, the values were similar in the tested slab prototypes. In any case, B4400 presented smaller values, which can be justified by the existence of a branch subjected to pure bending (if self-weight is disregarded, which is acceptable for this discussion), and the higher probability of having weaker sections (deficiencies on the local mechanical properties of FRC and/or steel profiles).

Regarding the shear capacity, it is verified that it significantly exceeds the flexural capacity (S800 and S1200), so shear failure never occurs for the present material-structural configuration of the PreSlabTec.

4.2. Strain measurement

Fig. 5 shows the force versus the compressive strains measured in the strain gauges indicated in Fig. 2 for the tested prototypes. Fig. 5a evidences that the compressive strains in the top surface of the FRC of the B4400 prototype were identical in the girders and in the deck. This reveals that, despite the very small thickness and relatively large width of the central part of the FRC deck, the strain field is the one expected for a standard T cross section. Therefore, it seems possible the adoption of this assumption for the development of a relatively simple design model, as will be discussed in Section 6. The results also evidence that when the test was interrupted, the compressive strain was about 1.6 ‰, which means that FRC was still far from crushing.

In the B2400 prototype the SG1 and SG2 strain gauges are 200 mm from the loaded section, and each one is installed in the girders. Fig. 5b shows that the evolution of the strains in these SGs was almost equal, and linear with the applied load, with a maximum value of about 0.55‰.

In the S800 the SG1 and SG2 are 200 mm and 400 mm from the loaded section, and the maximum corresponding values are 0.06‰ and 0.52‰, respectively.

The SG1, SG2 and SG3 in the S1200 are 600 mm, 300 mm and 150 mm from the loaded section, but the SG3 is located in the right span, which is the smallest one, while the SG1 and SG2 are in the left span, the largest one (Fig. 2d). Due to the predominant direct load transference to the right support above a load level of about 340kN, the strain in the SG3 started decrease with the increase of load. The maximum compressive strain did not exceed 0.48‰.

Fig. 6 shows the force versus the tensile strains measured in the strain gauges bonded to the steel in the bottom surface of the girders of the tested prototypes (Fig. 2). Fig. 6a evidences that the steel yielded at the loaded section of the B4400 prototype, with a maximum tensile strain of about 13‰. In the B2400 prototype the evolution of the tensile strains with the applied load was equal in both SG3 and SG4 up to a load level of about 125 kN, above which the gradient was a little bit higher in the SG4 than in the SG3, indicating a larger evolution of damage in the right shear span. The maximum tensile strain was 1.69‰, which indicates that at sections 200 mm from the loaded section, the steel is starting yielding (steel at yield initiation: 289 MPa/200GPa = 1.445‰). Regarding both the S-type prototypes, the maximum tensile strain was 1.4‰, below the yield strain of the steel.

Based on the obtained data, the moment versus curvature ($M-\chi$) curves of each monitored cross section were constructed (Fig. 7). It is

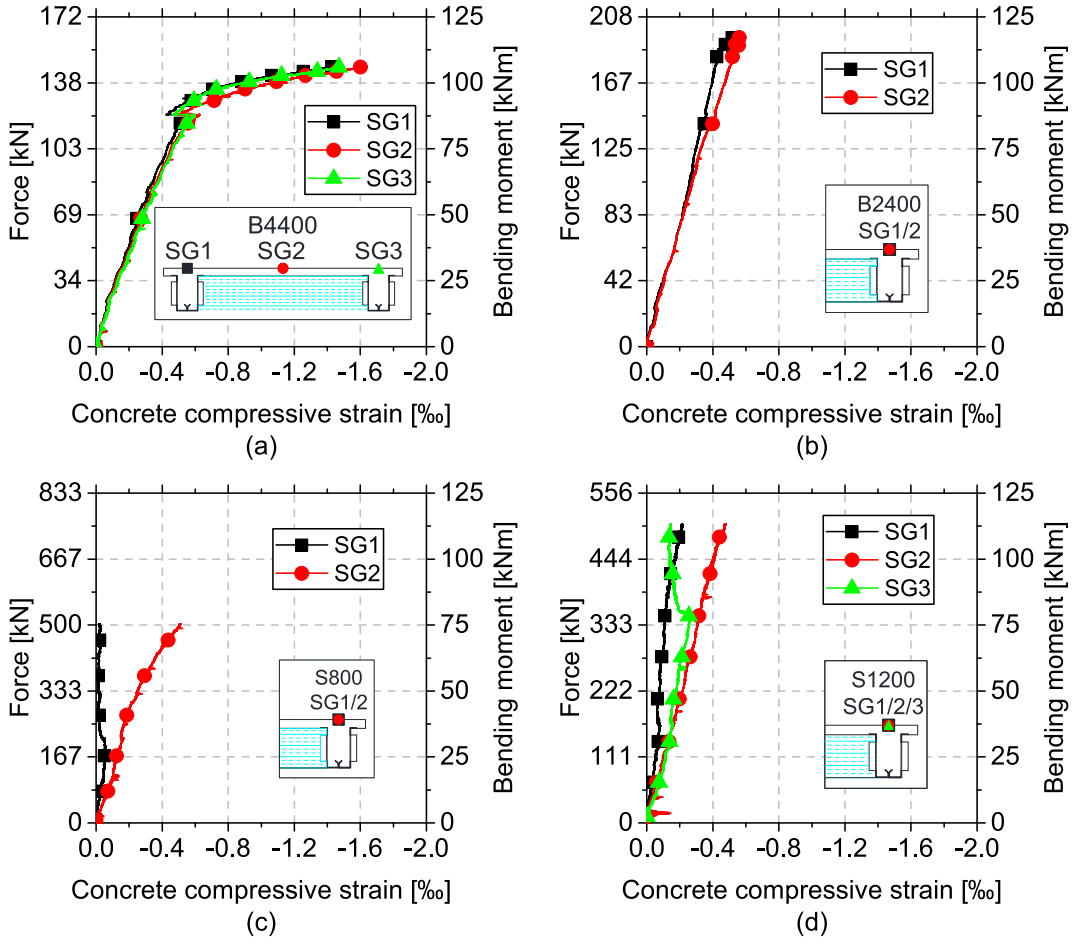

Fig. 5. Concrete strains: (a) Test B4400; (b) Test B2400; (c) Test S800 and (d) Test S1200.

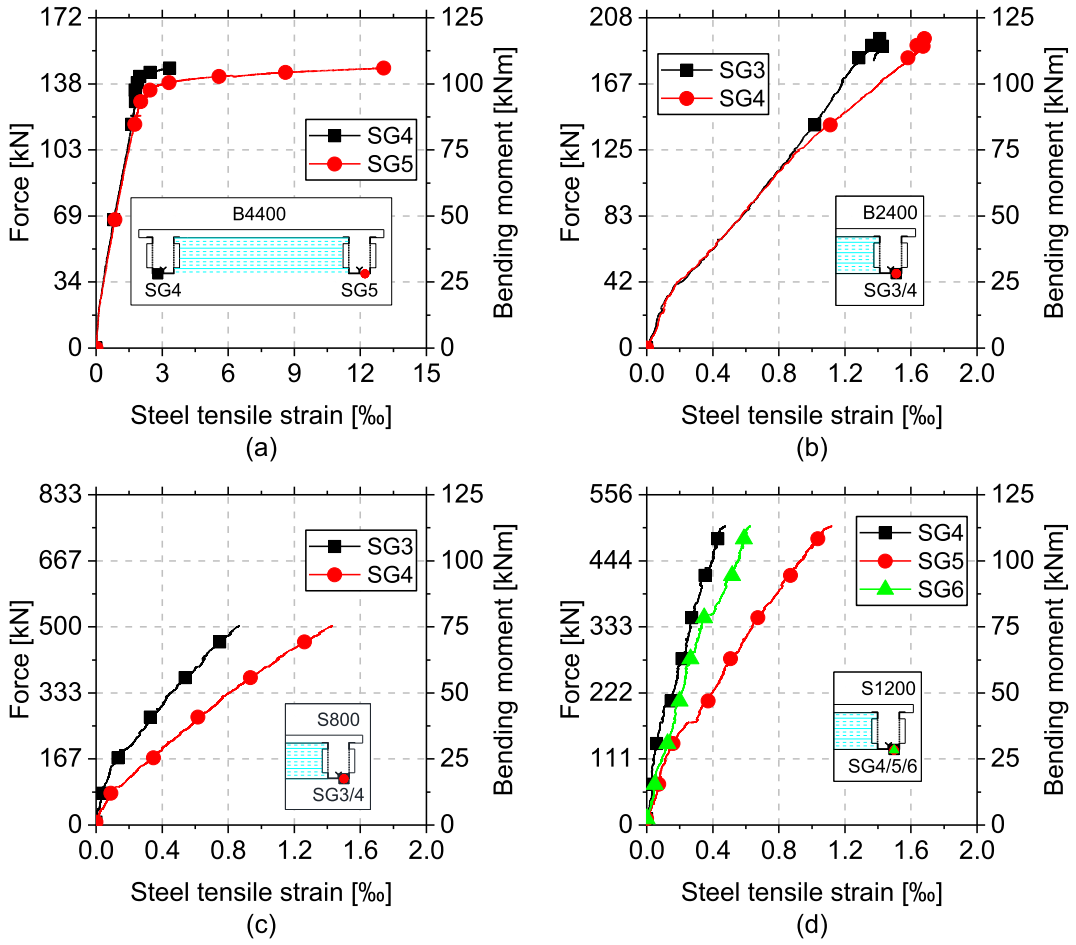

Fig. 6. Steel strains: (a) Test B4400; (b) Test B2400; (c) Test S800 and (d) Test S1200.

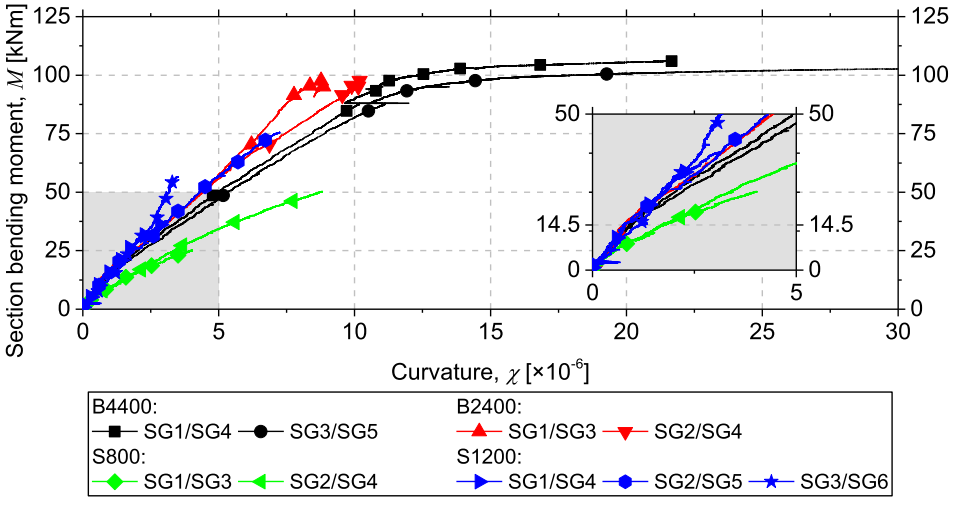

Fig. 7. Experimental moment–curvature curves.

concluded that, in general, the cross-sections monitored in three of the tests (B4400, B2400 and S1200) exhibit very similar $M-\chi$ response, particularly up to crack initiation (14.5 kNm, average value given in Table 7). In the S1200, the span in which the shear failure was expected to occur (SG3/SG6 section), a deviation was observed, due to the decrease of the strain in SG3 (see Fig. 5d) in consequence of a predominant direct load transference to the support.

On the other hand, in the S800 the monitored cross sections displayed considerably lower stiffness when compared to all other tests, which may indicate that in this case, the right support absorbed a much larger force than expected.

4.3. FRC stiffener strain evaluation

In one of the flexural tests (B2400) and both of the shear tests (S800 and S1200), the principal strains in the FRC composing the lateral

stiffener were appraised. These strains allow the detection of compression struts in the concrete, which usually precede the occurrence of a shear failure mode. The principal strains are calculated based on the monitorization of a couple rosettes installed in each test, as depicted in Fig. 2.

The adopted numbering and sign convention for the strains in the rosette, principal strains and their orientation are presented in Fig. 8. The maximum and minimum principal strains and corresponding angle are calculated from the following equations:

$$\varepsilon_{max,min} = \frac{\varepsilon_1 + \varepsilon_2 + \varepsilon_3}{3} \pm \frac{\sqrt{2}}{3}\sqrt{(\varepsilon_1 - \varepsilon_2)^2 + (\varepsilon_2 - \varepsilon_3)^2 + (\varepsilon_3 - \varepsilon_1)^2} \quad (4)$$

$$\theta = \frac{1}{2} tan^{-1}\left(\frac{\sqrt{3}(\varepsilon_3 - \varepsilon_2)}{2\varepsilon_1 - \varepsilon_2 - \varepsilon_3}\right) \quad (5)$$

To estimate the compressive stress (σ_c) from the measured compressive strain (minimum principal strain in the rosette, ε_{min}=ε_c), the parabola-rectangle diagram, as defined in Eurocode 2 [47] was adopted:

$$\sigma_c = \begin{cases} f_{cm}\left[1 - \left(1 - \frac{\varepsilon_c}{\varepsilon_{c2}}\right)^2\right] & \varepsilon_c \leqslant \varepsilon_{c2} \\ f_{cm} & \varepsilon_{c2} \leqslant \varepsilon_c \leqslant \varepsilon_{cu2} \end{cases} \quad (6)$$

where f_{cm} is the average concrete compressive strength (50 MPa was adopted), ε_{c2} is the strain at the point where the maximum compressive stress is reached (2.0‰ was adopted) and ε_{cu2} is the ultimate concrete compressive strain (3.5‰ was adopted).

Fig. 9 presents the evolution of the principal strains and their orientations in the B2400 test (positive and negative values represent, respectively, tension and compression strains). The relationship ε_{min}-ε_{max} during the loading process is shown in Fig. 9a, where it is visible that in the delta (Δ) rosette (closer to the loaded section) it was attained a maximum principal strain of 17.3‰ (much larger than the nominal steel yielding strain of about 289 MPa/200 GPa = 1.445‰) and a minimum principal strain of −2.2‰, which according to Eq. (3) conducts to a compressive stress of −45.5 MPa, quite close to the FRC average compressive strength. In the nabla (∇) rosette, the maximum principal strain state installed was significantly lower: a maximum principal strain of 1.26‰ (tensile) and a minimum principal strain of −0.85‰ (compressive), when the applied load was 187.7 kN (after the onset of yielding). These results suggest the critical shear region is close to the delta rosette or eventually between it and the loaded section (a non-monitored region), but yielding of the steel has occurred before an eventual shear failure occurrence.

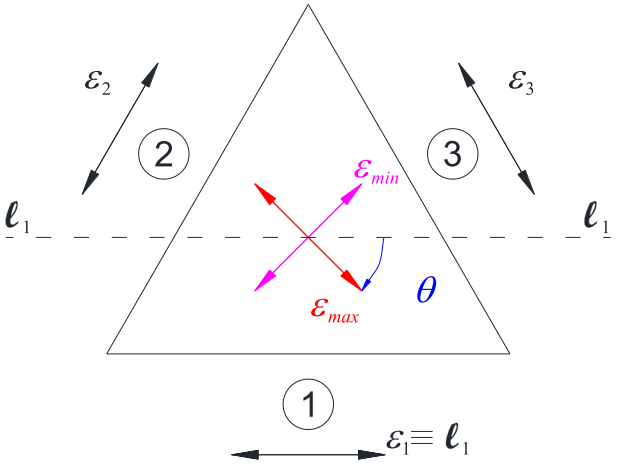

Fig. 8. Numbering and axis convention of the strain components and principal strains in a rosette.

Concerning the angle of the maximum principal strain, in the B2400 test, in the delta rosette, Fig. 9b shows that it maintained almost constant from cracking up to yield initiation, in about 40°, but for load levels above yield initiation, the angle of the maximum principal strain started decreasing up to have stabilized at about 10° by the end of the test. This decrease indicates the plastic hinge has spread to the region of this rosette. On the other hand, the nabla rosette shows a slightly different behaviour. The maximum principal strain orientation was around −20° at cracking, varying up to −40° at yielding initiation. At a load of 187.7 kN the maximum principal strain started inverting its orientation, getting an orientation of −10° at the end of the test, which suggests that the spread of the plastic hinge is attained in this rosette only above the indicated load level.

Fig. 10 shows that, in the S800 test the principal strains were smaller than 0.15‰, and the angle of the maximum principal strain has not exceeded 15° in the delta rosette and was higher than −30° in the nabla rosette. These results indicate this prototype was far away from failing in shear.

In the S1200 test (Fig. 11), more significant compressive strains in the FRC stiffener were mobilized compared to the previous test. In fact, although the maximum tensile strain was expected in the delta rosette, which is closer to the loaded section as well as closer to the tensile zone of the cross-section, the largest principal tensile strain was registered in the nabla rosette. The maximum compressive strain mobilized was only around 1‰, which is far from the strain necessary to produce a crushing strut.

5. Creep test

A creep bending test was also executed by subjecting a slab prototype to a uniformly distributed sustained load. The applied load was selected in order to replicate, as much as possible, the loading conditions of a residential building subjected to a design quasi-permanent combination action. According to Eurocode 0 [50], the quasi-permanent combination is evaluated as.

$$E_d = E\{G_{k,j}; P; \psi_{2,i} Q_{k,i}\} \quad (7)$$

where $G_{k,j}$ is the characteristic value of a permanent action$j$, P is the representative value of a prestress action (not applicable in the current case), $\psi_{2,i}$ is the factor for quasi-permanent value of a variable action (for residential and office areas this factor is 0.3), and $Q_{k,i}$ is the characteristic value of a variable action i.

In terms of permanent actions, the following actions are considered: the self-weight of the slab (2.215 kN/m^2) and an average estimated self-weight value of flooring and partitions (2.85 kN/m^2). On the other hand, in terms of variable actions, only the reference value for imposed loads on residential floors is considered (2 kN/m^2, as given in Eurocode 1 [51]). Since the slab prototype can replicate its own self-weight, a target additional uniformly distributed load of 2.85 + 0.3 × 2.0 = 3.45 kN/m^2 was established, which corresponds to a mid-span bending moment of 8.733 kNm/m (or 10.715 kNm when considering the total width of the slab prototype, 1227 mm).

Regarding the monitoring systems, 6 displacement transducers were installed in the slab prototype, 3 transducers per girder. In each girder, 2 transducers monitored the displacement of the sections at 1125 mm from each support (L/4), and one transducer monitored the displacement at mid-span (see Fig. 12). The test was performed in laboratory environment, with non-controlled temperature and relative humidity conditions, whose values were recorded along the test.

5.1. Loading

The effective additional load was applied by means of discrete masses distributed on the top surface of the slab prototype. A total mass of 1883 kg was used in this test and, by concentrating some of the

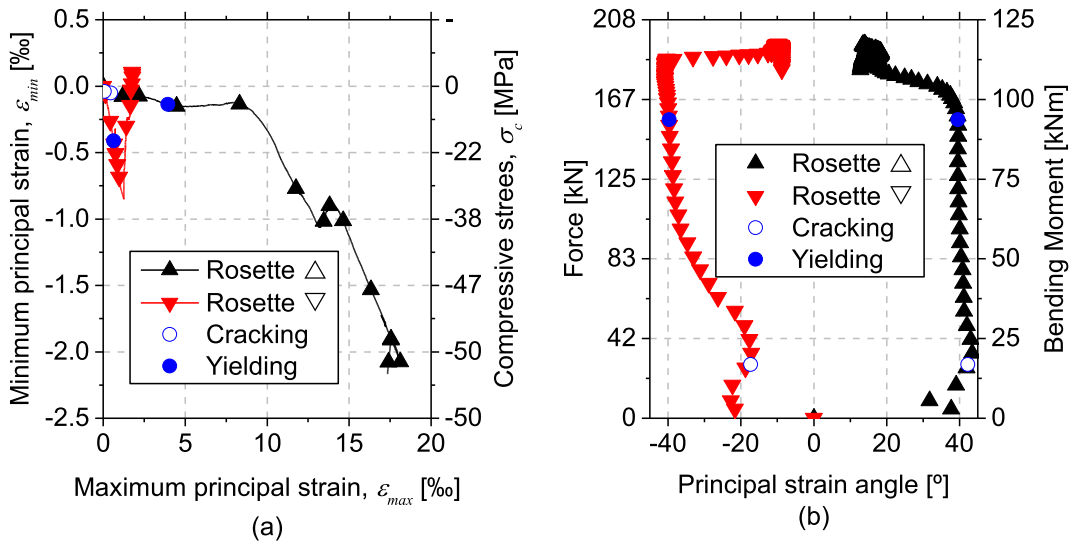

Fig. 9. B2400 test: (a) Minimum principal strain versus maximum principal strain and compressive stress, (b) Force and bending moment versus principal strain angle.

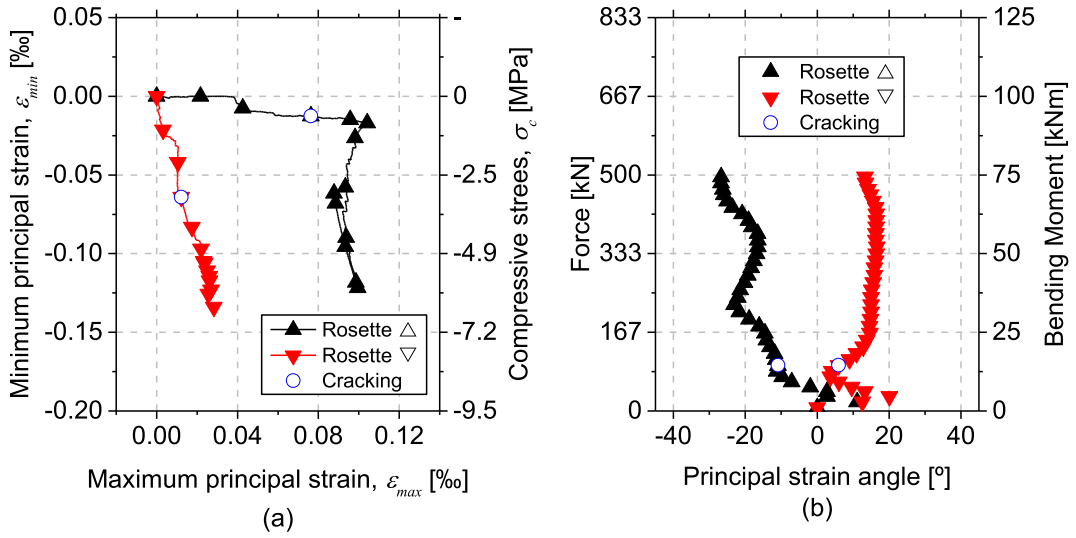

Fig. 10. S800 test: (a) Minimum principal strain versus maximum principal strain, (b) Force and bending moment versus principal strain angle.

heavier items on the central portion, an effective bending moment of 11.445 kNm was induced (corresponding to an equivalent uniformly distributed load of 3.685 kN/m^2). The prototype was loaded 65 days after its production.

Load was applied in approximately 40 min in three distinct phases: (1) 5 units of 90 kg weights; (2) 7 units of 42.5 kg weights and (3) 57 units of 20 kg weights. The instantaneous displacement values recorded in the different transducers in these phases are presented in Fig. 13.

5.2. Sustained loading

The load was maintained on the slab prototype for a total period of nearly 2500 h (about 100 days). During an initial period of about 1300 h, the displacements, ambient temperature and relative humidity were monitored continuously. After that, monitoring was suspended and resumed only a couple of days before unloading (all displacement transducers were kept in place during the suspension period). The obtained raw data is plotted in Fig. 14.

The evolution of one of the midspan transducers and corresponding ambient temperature within the time window defined in Fig. 14 is depicted in Fig. 15. This data clearly shows that the ambient temperature is directly correlated to the decrease of deflection in the prototype, which justified the correction of the original curves with temperature compensation coefficients. The obtained corrected displacements are presented in Fig. 16.

5.3. Unloading

At unloading, the deflection recovery of the prototype was monitored and the corresponding results are presented in Fig. 17a (the monitoring system was reset at the initiation of the unloading process, therefore null displacements are considered at this stage). While during loading the largest deformations were observed in the posterior girder (Girder 2: odd numbered LVDTs), during unloading the largest displacement recovery was observed in the frontal girder (Girder 1: even numbered LVDTs). In terms of average displacements, depicted in Fig. 17b, the variability between the ¼ span transducers was significantly lower compared to the loading stage.

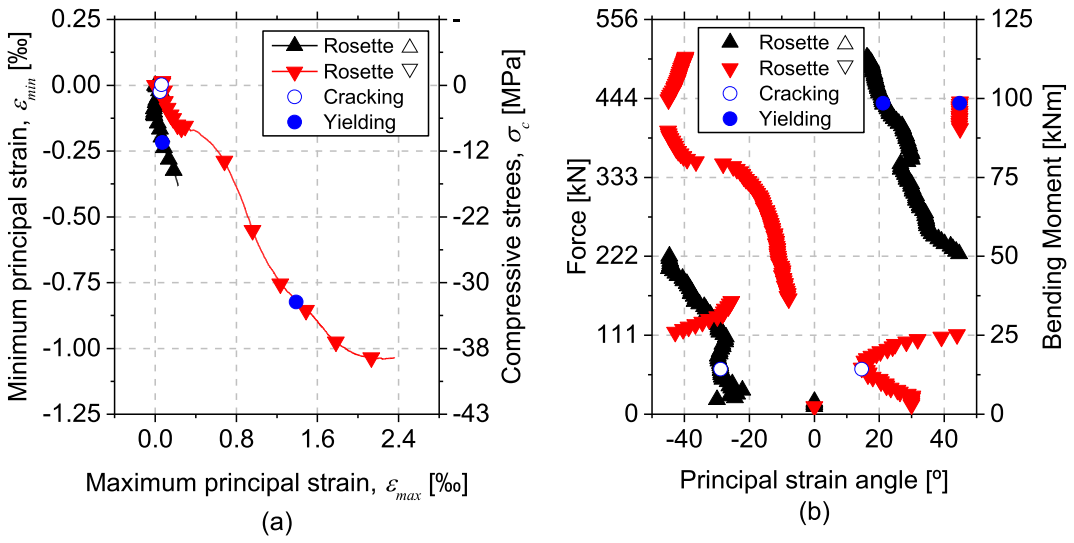

Fig. 11. S1200 test: (a) Minimum principal strain versus maximum principal strain, (b) Force and bending moment versus principal strain angle.

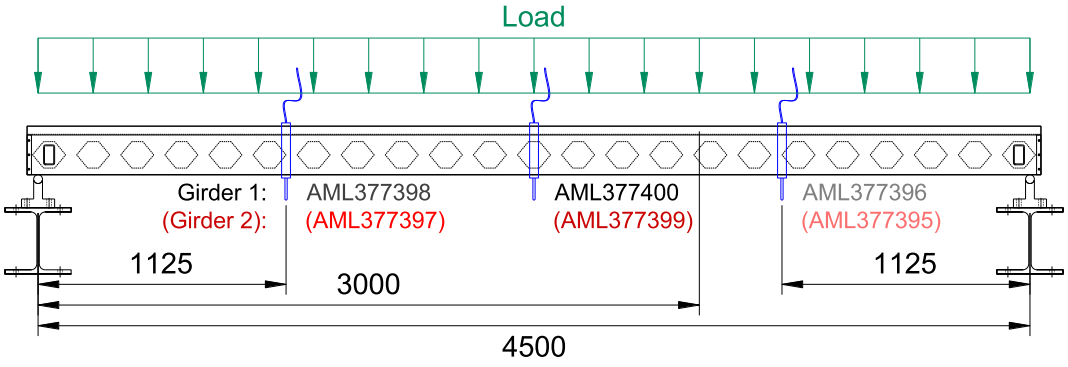

Fig. 12. Global monitoring system (dimensions in millimetres).

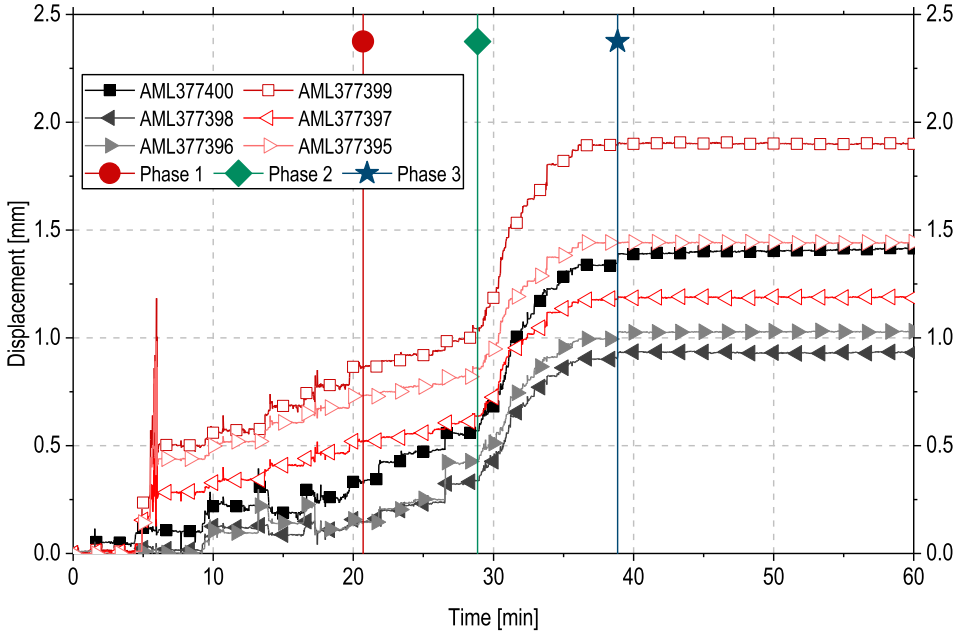

Fig. 13. Displacements measured during loading.

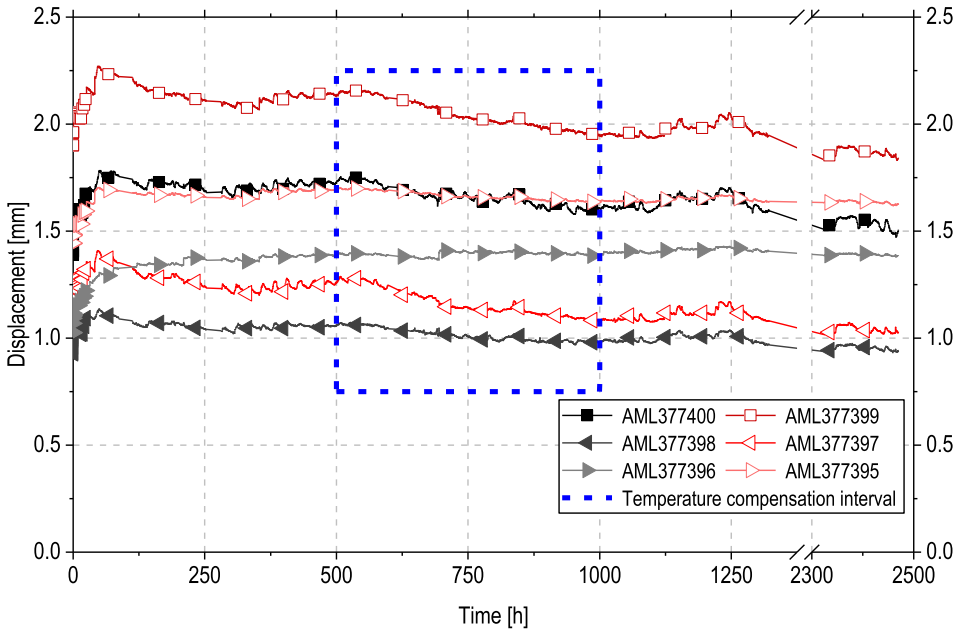

Fig. 14. Displacements during the sustained load period.

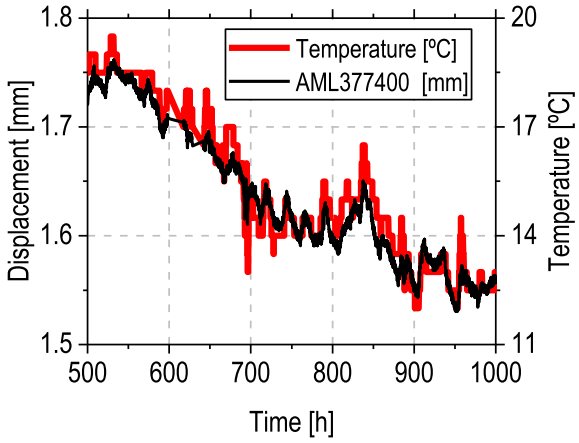

Fig. 15. Displacement in LVDT AML377400 and ambient temperature between 500 and 1000 h.

5.4. Analysis

Based on the results presented in Table 7, the applied bending moment in the creep test, 11.445 kNm (which does not take into account the self-weigh), is not expected to exceed the average cracking bending moment of the prototype, 14.5 kNm (in addition to the self-weight). Therefore, classic deflection equations may be used to estimate the expected deformation of the slab. For a beam subjected to a uniformly distributed load, the displacements at midspan and ¼ span are given by the following respective equations:

$$\delta(l/2) = \frac{5pl^4}{384EI} \tag{8}$$

$$\delta(l/4) = \frac{57pl^4}{6144EI} \tag{9}$$

Assuming the equivalent uniformly distributed load of 3.685 kN/m^2 (estimated value given in section 5.1), p may be approximated as 4.521 kN/m. The stiffness term, can be approximated as the average value obtained in Table 7 (EI=14437 kNm^2) and the span is 4500 mm.

Equations (8) and (9) provide an instantaneous deflection of 1.672 mm and 1.191 mm at midspan and at ¼ of the span, respectively. The error in relation to the experimentally obtained average values is 2% and 4%, respectively (Table 8), which demonstrates the good prediction capacity of these traditional equations for this structural composite system with this loading level. Concerning the deflection recovery, it was observed that the prototype exhibited a residual average deflection of approximately 30% (Table 8).

The creep coefficient, $\varphi(t, t_0)$, between the loading time t_0 and a given time increment t, can be determined from the following equation.

$$\varphi(t, t_0) = \frac{\delta_t - \delta_0}{\delta_0} \tag{10}$$

where δ_t is the total displacement at the time instant t, and δ_0 is the total instantaneous displacement. A summary of the obtained results is presented in Table 9.

Since the instantaneous deformation component measured during the tests does not account for the deformation due to the self-weigh, the values of $\delta_{0,exp}$ and $\delta_{t,exp}$ were corrected to reflect the correct total deformation. The corrected instantaneous deflection is denoted by $\delta'_{0,exp}$ while the deflection after t days is denoted by $\delta'_{t,exp}$.

The obtained creep coefficients for the individual LVDTs vary between 0.05 and 0.26. In terms of average values, both at midspan and at ¼ span, the average value of the coefficient is about 0.13, which is much smaller than the one obtained with the formulation of Eurocode 2 (approximately 0.74) when the theoretical exposed concrete perimeter (u) is considered (u = 1227 mm). The real exposed concrete perimeter was, in reality, smaller than this value since almost the total top surface of the slab was covered by the loading masses. However, even assuming the minimum theoretical u value in this context, the creep coefficient exceeds 0.5, which is still higher than the experimentally recorded value, indicating that this approach overestimates this coefficient.

6. Software for design of the PreSlabTec slab system

6.1. User interface

A numerical tool was developed to assist the structural design of the PreSlabTec slab system for various load and geometry conditions. Based

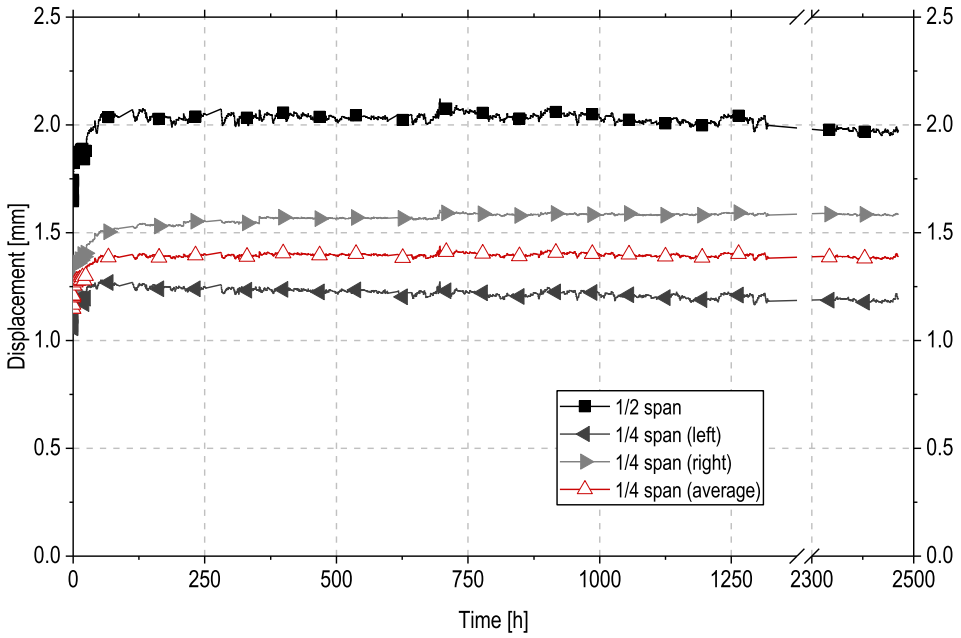

Fig. 16. Average displacements during the sustained load period.

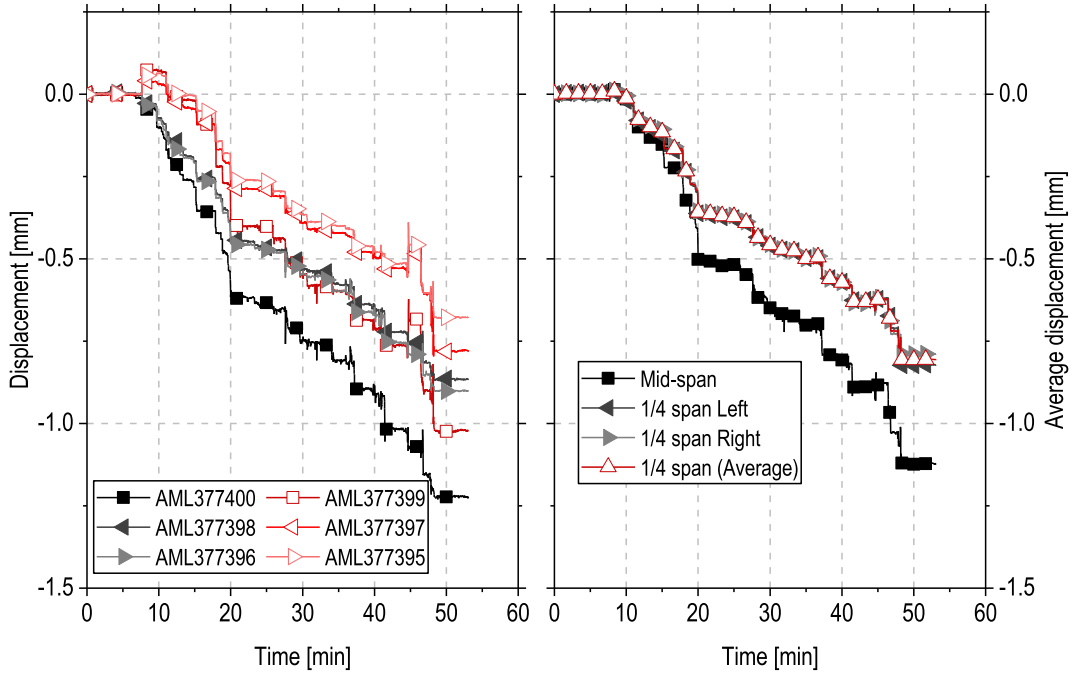

Fig. 17. Displacements measured during the unloading operation: (a) Displacement transducer measurements, (b) average displacement results.

on the available set of slab configurations and considering the slab's span and acting loads, the software performs the ultimate (ULS) and serviceability limit states (SLS) safety verifications according to the design recommendations and rules of Eurocode 2 [47] and *fib* Model Code 2010 [48].

The interface of the software is presented in Fig. 18. One of its main functionalities is the possibility to run the SLS and ULS safety verifications for all the available configurations of the PreSlabTec slabs, given the slab's span and loads acting on the slab.

6.2. Theoretical approach

The software has the following aspects:

i. It includes a database file with the data of each PreSlabTec slab configuration, namely: geometry, material properties and the flexural response (curvature vs resisting bending moment vs neutral axis position, $\chi - M - na$) for the SLS and ULS conditions. The flexural response, namely the moment vs curvature ($M - \chi$) of each different type of cross section of the available PreSlabTec configurations is determined with the software DOCROS [49] by considering the constitutive models for the SFRC and steel components according to the MC2010 design recommendations [48];
ii. The self-weight of each slab configuration is determined considering the geometry and materials density;
iii. The structure is discretized in nodes and bars considering the span of the slab and the position of the openings in the webs of the

Table 8
Instantaneous displacements of the slab prototype at loading and unloading.

LVDT	Experimental values		
	$\delta_{loading}$	$\delta_{unloading}$	$\%\delta$
AML377400	1.389	1.220	12%
AML377399	1.902	1.024	46%
AML377398	0.932	0.866	7%
AML377397	1.190	0.780	34%
AML377396	1.026	0.900	12%
AML377395	1.443	0.680	53%
½ span	1.646	1.122	32%
¼ span	1.147	0.806	30%

$\%\delta$ is the residual displacement of the slab prototype, given by $(\delta_{loading} - \delta_{unloading})/\delta_{loading} \times 100\%$.

Table 9
Experimental creep coefficient for $t = 100$ days of loading and $t_0 = 65$ days.

LVDT	Displacements [mm]				$\varphi(100,65)_{exp}$
	$\delta_{0,exp}$	$\delta_{100,exp}$	$\delta'_{0,exp}$	$\delta'_{100,exp}$	
AML377400	1.389	1.806	2.224	2.641	0.19
AML377399	1.902	2.130	3.045	3.273	0.07
AML377398	0.932	1.073	1.492	1.633	0.09
AML377397	1.190	1.290	1.905	2.005	0.05
AML377396	1.026	1.453	1.643	2.070	0.26
AML377395	1.443	1.719	2.310	2.586	0.12
½ span	1.646	1.968	2.635	2.957	0.12
¼ span	1.147	1.384	1.838	2.073	0.13

$\delta'_{0,exp} = \delta_{0,exp} + c{\cdot}\delta_{0,exp}$ and $\delta'_{100,exp} = \delta_{100,exp} + c{\cdot}\delta_{0,exp}$, where the constant c is 0.6, estimated from the ratio between the nominal self-weight of the prototype (2.215 kN/m^2) and the effective uniformly applied load, 3.685kN/m^2.

steel longitudinal girders. As presented in Fig. 19, each bar is discretized by two nodes, with two degrees of freedom per node: vertical displacement (u_1) and rotation ($\theta_2 = u_2$). For each bar is assigned a cross-section type for the steel girders as presented in Fig. 20, namely: S1 – girder without the opening in the web, S2 to S5 – girder with openings in the web. For each cross-section type (S1 to S5), the data base indicated in step i) includes the corresponding $M-\chi$, from which the flexural stiffness is obtained and used in Eq. (11) for the evaluation of the secant (or tangent) stiffness matrix of the elements discretizing the slab;

iv. According to the loads acting in the slab, the software determines the load combinations according to the Eurocode 0 [50] to be used in the SLS and ULS safety verifications;
v. Based on the matrix displacement method, the incremental generalized displacements of the nodes of the structure ($\underline{\Delta u}$) are determined considering the stiffness (secant or tangent are options in the software) matrix of the slab ($\underline{K}$) and the incremental generalized nodal forces on the structure ($\underline{\Delta F}$), namely:

$$\underline{K}\cdot\underline{\Delta u} = \underline{\Delta F} \tag{11}$$

The stiffness matrix of each bar is determined considering the Timoshenko beam theory, admitting the reduced shear area (A_{red}, Fig. 21) is determined from the equation:

$$A_{red} = A_1 + \beta{\cdot}A_2 \tag{12}$$

where A_1 is the area of the FRC in compression, A_2 is the area of FRC in tension (Fig. 21),$\beta = 1 - \varepsilon_t/\varepsilon_u$, with ε_t being the tensile strain and $\varepsilon_u = 2\%$ the ultimate tensile strain for SFRC slab submitted to bending;

vi. The shear resistance of the PreSlabTec slab is determined for ULS conditions. The model is based on the Variable Engagement Model and Simplified Modified Compression Field Theory adopted in MC2010 to determine the shear resistance of FRC structural elements, which is presented elsewhere [52,53]. The steel webs of the slab's girders are considered as transverse reinforcement. However, its contribution is limited to the minimum resistance provided by the steel area in the section in shear (S_s) and in section in tension (S_t) in the vicinity of a critical diagonal shear crack, as illustrated in Fig. 22;
vii. The results of the SLS and ULS safety verifications are displayed in the results window, including the graphical output of the vertical displacement profile of the slab for SLS conditions, and the bending moment and shear force diagrams for ULS

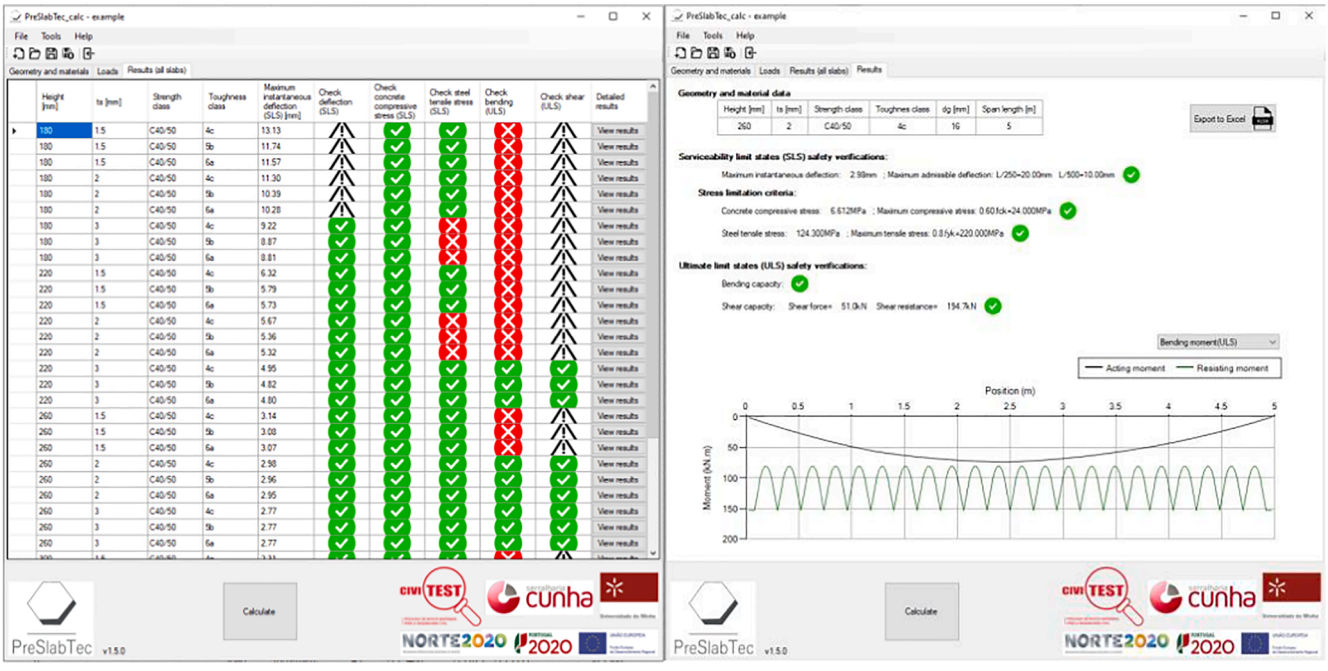

Fig. 18. User interface of the software.

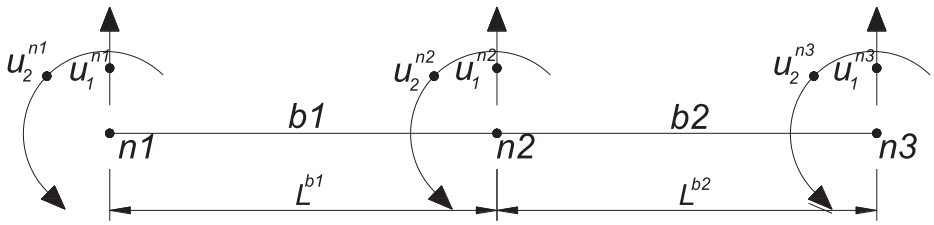

Fig. 19. Discretization of structure in bars of two nodes (two degrees of freedom per each node).

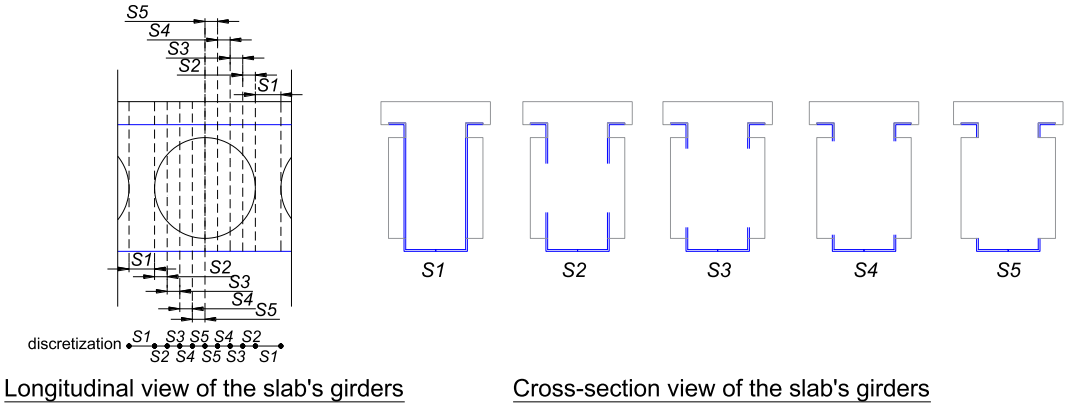

Fig. 20. Assignment of cross-section type for each bar.

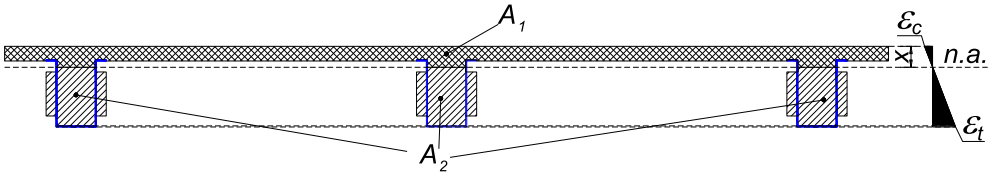

Fig. 21. Determination of the reduced shear area.

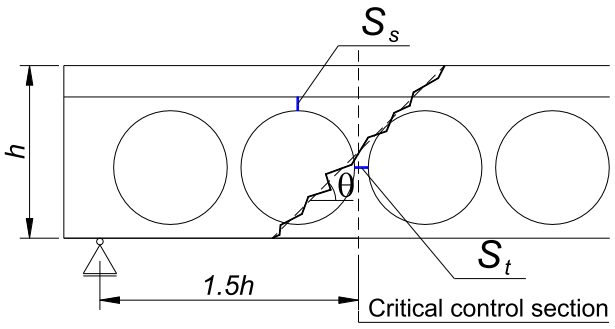

Fig. 22. Determination of the minimum steel area that contributes to the slab's shear resistance.

conditions. It is also given the possibility to export the results to an excel format file.

6.3. Assessment of the predictive performance of the software

The predictive performance of the software was assessed by comparing the force vs. deflection relationship with the experimental results of PreSlabTec slab submitted to 4-point bending (B4400) presented in Section 4.

To simulate the flexural response of the slab, the average values of material properties indicated in Section 3 were used for defining the constitutive models of the SFRC and steel components. Additionally, partial safety factors equal to 1.0 are considered for the materials.

Fig. 23 presents the moment vs. curvature and force vs. deflection response obtained from the software (numerical) and registered experimentally (experimental) for the 4-point bending test. The results show that the software could capture with acceptable accuracy for design purposes both the $M-\chi$ and the $F-u$ relationships. Regarding this last one, the predictive performance was excellent up to yield initiation of the steel component. Since the numerical approach is controlled in force, when the bending moment in a certain element attains the maximum value of the flexural capacity of the corresponding slab's cross section, the flexural stiffness is assumed almost null for the element representative of this moment–curvature response (Fig. 23a), which leads to the localization of a plastic hinge in this element, conducting to the plateau observed for the numerical $F-u$ relationship in Fig. 23b.

7. Conclusions

In this paper a new pre-fabricated lightweight slab system for residential and commercial buildings was proposed, and its structural performance at serviceability and ultimate limit state conditions (SLS and ULS, respectively) was assessed by performing experimental tests with representative prototypes. From the experimental tests the following observations can be pointed out:

(1) The prototypes tested in flexural loading conditions, one under 4 points, B4400, and the other under 3 points, B2400, both

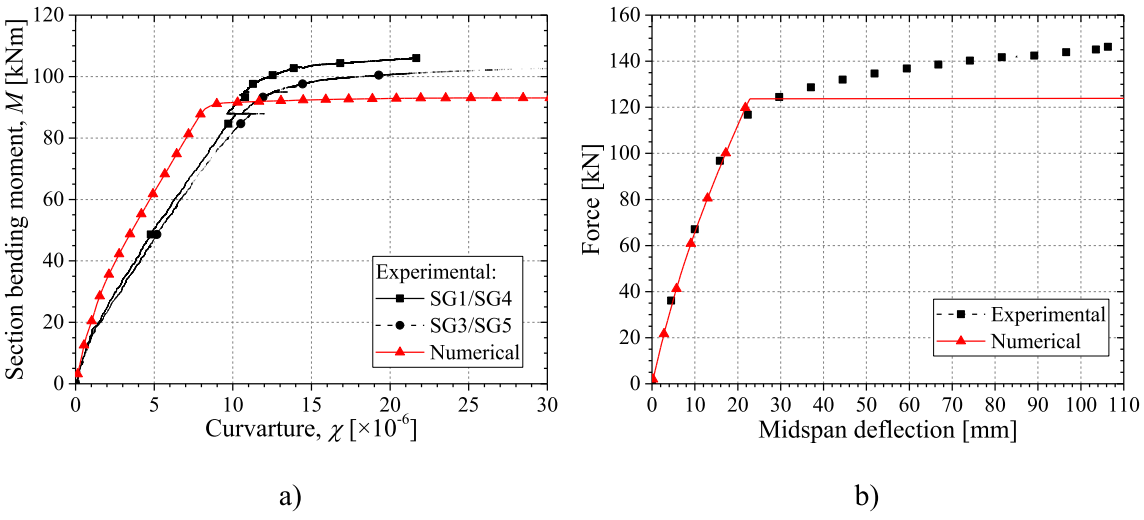

Fig. 23. Moment-curvature (a) and force–deflection (b) in the B4400 prototype registered experimentally and obtained numerically.

presented a very ductile behaviour, by mobilizing the tensile capacity of the cold formed steel sheets of the longitudinal girders, without signs of crushing of the fibre reinforced concrete (FRC). An average elastic flexural stiffness (EI_{el}), bending moment at crack initiation (M_{cr}) and at yield initiation (M_y) of, respectively, 15,754 kN/m2, 14.65 kNm and 87.4 kNm were obtained, while the maximum flexural capacity was 117.3 kNm. The force–deflection response of these prototypes was composed by a linear phase, followed by an elasto-cracked stage of relatively high amplitude and small loss of stiffness up to the yield initiation of the longitudinal steel profiles, with subsequent hardening phase of very ductile behaviour. If the maximum load supported by the B4400 prototype is converted in a uniform distributed load (inducing the same maximum bending moment), a live load approximately 44kN/m2 is obtained. For the flexural stiffness of these prototypes, and considering a load combination for SLS conditions of 7kN/m2 (which includes a live load of 2kN/m2), a maximum span of about 8.0 m can be supported by respecting the SLS and ULS conditions. The self-weight of this slab is 210 kg/m2, composed by 0.08 m2/m2 of FRC and 18.21 kg/m2 of cold formed steel profiles;

(2) Despite the adoption of loading conditions for inducing shear failure in the S800 and S1200 prototypes, shear failure never occurred, revealing the very effective resisting shear mechanisms assured by the FRC crossing the openings executed in the longitudinal steel girders. This is also supported by the maximum principal strains measured in the web's lateral face of the longitudinal girders in the S1200 prototype, where the steel yield strain was exceeded ;

(3) For the prototype submitted to a permanent bending loading configuration recommended by Eurocode 0 for slabs of residential buildings, an average creep coefficient of 0.13 was obtained, which is significantly smaller than the one determined by the Eurocode 2 formulation. Research on this specific phenomenon should be developed for deriving a dedicated formulation on the creep of this material-structural system;

(4) A dedicated user-friendly software was developed for the design of PreSlabTec slabs, based on a theoretical approach that combines the moment–curvature relationship for the types of sections composing a PreSlabTec slab and the matrix displacement method. The good predictive performance of this approach was demonstrated by simulating the force–deflection registered in the B4400.

Numerical simulations with software based on the finite element method are being carried out for extending the potentialities of PreSlabTec for larger spans and also for assessing its performance under dynamic loading conditions.

CRediT authorship contribution statement

Joaquim A.O. Barros: Conceptualization, Methodology, Supervision, Formal analysis, Writing – original draft. **Inês G. Costa:** Methodology, Formal analysis, Writing – review & editing, Visualization. **Cristina M.V. Frazão:** Investigation, Writing – review & editing. **Tiago D.S. Valente:** Software, Writing – review & editing. **Lúcio A.P. Lourenço:** Conceptualization, Writing – review & editing. **Felipe J.S.A. Melo:** Investigation, Writing – review & editing.

Declaration of Competing Interest

The authors declare that they have no known competing financial interests or personal relationships that could have appeared to influence the work reported in this paper.

Acknowledgements

The authors would like to acknowledge the financial support provided by the 'Incentive System for Business R&DT – Demonstration Projects in Co-Promotion and co-financing by the ERDF – European Regional Development Fund', through NORTE 2020 (NORTE-01-0247-FEDER-033690).

References

[1] Nayar S.K., Gettu R. Comparison of different design methodologies for FRC slabs-on-grade. 8th RILEM International Symposium on Fiber Reinforced Concrete: challenges and opportunities (BEFIB 2012). Guimarães, Portugal, 19–21 September. 2012; 1070–1081.

[2] Nobili A, Lanzoni L, Tarantino AM. Experimental investigation and monitoring of a polypropylene-based fiber reinforced concrete road pavement. Constr Build Mater 2013;47:888–95. https://doi.org/10.1016/j.conbuildmat.2013.05.077.

[3] R. Gettu, B. Barragán, T. García, G. Ramos, C. Fernández, R. Oliver, Steel fiber reinforced concrete for the Barcelona metro line 9 tunnel lining, Proceedings of the 6th International RILEM Symposium on Fibre-Reinforced Concretes (FRC) (BEFIB 2004), Varenna, Italy, 20-22 September, 2004, RILEM Publications S.A.R.L., 141-156.

[4] Caratelli Angelo, Meda Alberto, Rinaldi Zila, Romualdi Paolo. Structural behaviour of precast tunnel segments in fiber reinforced concrete. Tunn Undergr Space Technol 2011;26(2):284–91. https://doi.org/10.1016/j.tust.2010.10.003.

[5] Tiberti G, Minelli F, Plizzari G. Reinforcement optimization of fiber reinforced concrete linings for conventional tunnels. Compos B Eng 2014;58(2014):199–207. https://doi.org/10.1016/j.compositesb.2013.10.012.

[6] Carmona S, Molins C, Aguado A, Mora F. Distribution of fibers in SFRC segments for tunnel linings. Tunn Undergr Space Technol 2016;51:238–49. https://doi.org/10.1016/j.tust.2015.10.040.

[7] de la Fuente A, Escariz R, de Figueiredo AD, Aguado A. Design of macro-synthetic fiber reinforced concrete pipes. Constr Build Mater 2013;43:523–32. https://doi.org/10.1016/j.conbuildmat.2013.02.036.

[8] Soetens T., Design Models for the Shear Strength of Prestressed Precast Steel Fibre Reinforced Concrete Girders. Doctoral thesis. Belgium:Ghent University; 2015. https://doi.org/10.13140/RG.2.1.2015.6968.

[9] Mazaheripour H, Barros JAO, Soltanzadeh F, Sena-Cruz J. Deflection and cracking behavior of SFRSCC beams reinforced with hybrid prestressed GFRP and steel reinforcements. Eng Struct 2016;125:546–65. https://doi.org/10.1016/j.engstruct.2016.07.026.

[10] B. Parmentier, P. Van Itterbeeck, A. Skowron, The flexural behaviour of SFRC flat slabs: the Limelette full-scale experiments for supporting design model codes, Proceedings of the FRC 2014 Joint ACI-fib International Workshop, Montréal, Canada, 24-25 July, 2014, J. P. Charron, B. Massicotte, B. Mobasher and G. A. Plizzari (Eds), ACI-fib.

[11] B. Mobasher, J.A.O. Barros, A.E. Naaman, X. Destree et al., Report on Design and Construction of Steel Fiber-Reinforced Concrete Elevated Slabs, ACI 544.6R-15, Reported by ACI Committee 544, 2015.

[12] Nogales Alejandro, de la Fuente Albert. Numerical-aided flexural-based design of fibre reinforced concrete column-supported flat slabs. Eng Struct 2021;232:111745. https://doi.org/10.1016/j.engstruct.2020.111745.

[13] Crocetti R, Sartori T, Tomasi R. Innovative Timber-Concrete Composite Structures with Prefabricated FRC Slabs. J Struct Eng 2015;141(9):04014224. https://doi.org/10.1061/(ASCE)ST.1943-541X.0001203.

[14] Sousa C, Barros JAO, Correia JRR, Valente TDS. Development of sandwich panels for multi-functional strengthening of RC buildings: characterization of constituent materials and shear interaction of panels assemblies. Constr Build Mater 2021;267:120849. https://doi.org/10.1016/j.conbuildmat.2020.120849.

[15] Barragán BE. Failure and toughness of steel fiber reinforced concrete under tension and shear. Doctoral thesis. Barcelona, Spain: Universitat Politecnica de Catalunya; 2002.

[16] Minelli F., Plain and Fiber Reinforced Concrete Beams under Shear Loading: Structural Behavior and Design Aspects. Doctoral thesis. Starrylink Editor. Italy: Department of Civil Engineering, University of Brescia; 2005.

[17] Aoude H, Belghiti M, Cook WD, Mitchell D. Response of Steel Fiber-Reinforced Concrete Beams with and without Stirrups. ACI Struct J 2012;109(3):359–68.

[18] Conforti A, Minelli F, Plizzari GA. Wide-shallow beams with and without steel fibres: a peculiar behaviour in shear and flexure. Compos B Eng 2013;51:282–90. https://doi.org/10.1016/j.compositesb.2013.03.033.

[19] Jain K, Singh B. Deformed steel fibres as minimum shear reinforcement - An investigation. Structures 2016;7:126–37. https://doi.org/10.1016/j.istruc.2016.06.003.

[20] Amin A, Foster SJ. Shear strength of steel fibre reinforced concrete beams with stirrups. Eng Struct 2016;111:323–32. https://doi.org/10.1016/j.engstruct.2015.12.026.

[21] Toutanji H, Deng Y. Deflection and crack-width prediction of concrete beams reinforced with glass FRP rods. Constr Build Mater 2003;17(1):69–74. https://doi.org/10.1016/S0950-0618(02)00094-6.

[22] Ahmed Ehab A, Benmokrane Brahim, Sansfaçon Maxime. Case study: design, construction, and performance of the La Chancelière Parking garage's concrete flat slabs reinforced with GFRP bars. J Compos Constr 2017;21(1):05016001. https://doi.org/10.1061/(ASCE)CC.1943-5614.0000656.

[23] Manalo A, Benmokrane B, Park K-T, Lutze D. Recent developments on FRP bars as internal reinforcement in concrete structures. Concrete in Australia 2014;40(2):46–56.

[24] *fib* bulletin 40, FRP reinforcement in RC structures, Technical Report, ISBN: 978-2-88394-080-2, 2007, 160 pages, https://doi.org/10.35789/fib.BULL.0040.

[25] ACI Committee 440, Guide for the Design and Construction of concrete reinforced with FRP bars, ACI 440.1R-06, American Concrete Institute, Farmington Hills, MI, USA, 2001.

[26] Canadian Standards Association, Design and Construction of Building Components with Fibre-Reinforced polymers. CAN/CSA S806-02, Rexdale, Ontario, Canada.

[27] Solyom S, Di Benedetti M, Guadagnini M, Balázs GL. Effect of temperature on the bond behaviour of GFRP bars in concrete. Compos B Eng 2020;183:10. https://doi.org/10.1016/j.compositesb.2019.107602.

[28] Rosa IC, Firmo JP, Correia JR, Barros JAO. Bond behaviour of sand coated GFRP bars to concrete at elevated temperature – Definition of bond vs. slip relations. Compos B Eng 2019;160:329–40.

[29] Aiello MA, Ombres L. Structural performances of concrete beams with hybrid (fiber-reinforced polymer-steel) reinforcements. J Compos Constr 2002;6(2):133–40.

[30] Leung H, Balendran R. Flexural behaviour of concrete beams internally reinforced with GFRP rods and steel rebars. Structural Survey 2003;21(4):146–57.

[31] Qu Wenjun, Zhang Xiaoliang, Huang Haiqun. Flexural Behavior of Concrete Beams Reinforced with Hybrid (GFRP and Steel) Bars. J Compos Constr 2009;13(5):350–9.

[32] Lau Denvid, Pam Hoat Joen. Experimental study of hybrid FRP reinforced concrete beams. Eng Struct 2010;32(12):3857–65.

[33] Alsayed Saleh H, Alhozaimy Abdulrahman M. Ductility of concrete beams reinforced with FRP bars and steel fibers. J Compos Mater 1999;33(19):1792–806.

[34] Issa Mohamed S, Metwally Ibrahim M, Elzeiny Sherif M. Influence of fibers on flexural behavior and ductility of concrete beams reinforced with GFRP rebars. Eng Struct 2011;33(5):1754–63.

[35] Wang Huanzi, Belarbi Abdeldjelil. Ductility characteristics of fiber-reinforced-concrete beams reinforced with FRP rebars. Constr Build Mater 2011;25(5):2391–401.

[36] Yang J-M, Min K-H, Shin H-O, Yoon Y-S. Effect of steel and synthetic fibers on flexural behavior of high-strength concrete beams reinforced with FRP bars. Compos B Eng 2012;43(3):1077–86. https://doi.org/10.1016/j.compositesb.2012.01.044.

[37] Youssef MH, Ahmed EA, Benmokrane B. Structural Behavior of GFRP-RC Bridge Deck Slabs Connected with UHPFRC Joints under Flexure and Shear. ASCE J Bridge Eng 2019;24(9):04019092. https://doi.org/10.1061/(ASCE)BE.1943-5592.0001475.

[38] Wang L, Weiqing L, Wan L, Fang H, Hui D. Mechanical performance of foam-filled lattice composite panels in four-point bending: Experimental investigation and analytical modeling. Compos B Eng 2014;67:270–9. https://doi.org/10.1016/j.compositesb.2014.07.003.

[39] Reis EM, Rizkalla SH. Material characteristics of 3-D FRP sandwich panels. Constr Build Mater 2008;22(6):1009–18. https://doi.org/10.1016/j.conbuildmat.2007.03.023.

[40] Fam A, sharaf T. Flexural performance of sandwich panels comprising polyurethane core and GFRP skins and ribs of various configurations. Compos Struct 2010;92:2927–35. https://doi.org/10.1016/j.compstruct.2010.05.004.

[41] G. Sopal, S. Rizkalla, G. Solomon, Performance of new 3D GFRP sandwich panels with corrugated GFRP sheets, Proceedings of the Conference on FRP Composites in Civil Engineering (CICE 2012), Rome, Italy, 13-15 June, 2012.

[42] Abdolpour H, Garzón-Roca J, Escusa G, Sena-Cruz JM, Barros JAO, Valente MIB. Composite modular floor prototype for emergency housing applications: Experimental and analytical approach. J Compos Mater 2018;52(13):1747–64. https://doi.org/10.1177/0021998317733318.

[43] Mastali M, Valente MIB, Barros JAO. Flexural performance of innovative hybrid sandwich panels with special focus on the shear connection behavior. Compos Struct 2017;160:100–17. https://doi.org/10.1016/j.compstruct.2016.10.066.

[44] Mastali M, Valente MIB, Barros JAO, Gonçalves DMF. Development of innovative hybrid sandwich panel: Experimental results. Compos Struct 2015;133:476–98. https://doi.org/10.1016/j.compstruct.2015.07.114.

[45] Gonilha JA, Barros JAO, Correia JR, Sena-Cruz JM, Branco FA, Ramos LR, Gonçalves DMF, Alvim MR, Santos T. Static, dynamic and creep behaviour of a full-scale GFRP-SFRSCC hybrid footbridge. Compos Struct 2014;118:496–509. https://doi.org/10.1016/j.compstruct.2014.08.009.

[46] Kaszubska M, Kotynia R, Barros JAO, Baghi H. Shear behavior of concrete beams reinforced exclusively with longitudinal glass fiber reinforced polymer bars: Experimental research. Struct. Concrete 2018;19(1):152–61. https://doi.org/10.1002/suco.201700174.

[47] European Committee for Standardization, Eurocode 2: Design of concrete structures Part 1-1: General rules and rules for buildings, vol. NP EN 1992-1-1: 2010.

[48] *fib*-federation internationale du beton, fib Model Code for Concrete Structures 2010, John Wiley & Sons, 2013.

[49] C.A.A. Basto, J.A.O. Barros, Numeric simulation of sections submitted to bending, Department of Civil Engineering, School of Engineering, University of Minho, Guimarães, Portugal, Technical Report 08-DEC/E-46, 2008, https://doi.org/10.13140/RG.2.1.2452.2723.

[50] European Committee for Standardization, Eurocode 0: Basis of structural design, vol. NP EN 1990:2009.

[51] European Committee for Standardization, Eurocode 1: Actions on structures Part 1-1: General actions – Densities, self-weight, imposed loads for buildings, vol. NP EN 1991-1-1: 2009.

[52] Valente T D S, Barros J A O, Moraes-Neto B N, Moussa Y H. Appraisal of MC2010 shear resistance approaches coupled with a residual flexural strength prediction model. IOP Conf Ser Mater Sci Eng 2019;596(1):012004. https://doi.org/10.1088/1757-899X/596/1/012004.

[53] Valente T. Advanced tools for design and analysis of fiber reinforced concrete structures. Doctoral thesis. Guimarães, Portugal: University of Minho; 2019.